PNAS RESEARCH ARTICLE | PHYSICS

Photovoltaic effect by soft phonon excitation

Yoshihiro Okamura[a,1,2], Takahiro Morimoto[a,b,1], Naoki Ogawa[a,c], Yoshio Kaneko[c], Guang-Yu Guo[d,e], Masao Nakamura[c], Masashi Kawasaki[a,c], Naoto Nagaosa[a,c], Yoshinori Tokura[a,c,f], and Youtarou Takahashi[a,c,2]

Edited by Angel Rubio, Max-Planck-Institut für Struktur und Dynamik der Materie, Hamburg, Germany; received December 9, 2021; accepted February 20, 2022

Photodetection is an indispensable function of optoelectronic devices in modern communication and sensing systems. Contrary to the near-infrared/visible regions, the fast and sensitive photodetectors operated at room temperature for the far-infrared/terahertz regions are not well developed despite a possibly vast range of applications. The bulk photovoltaic effect (BPVE) in single-phase, noncentrosymmetric materials based on the shift current mechanism enables less-dissipative energy conversion endowed with instantaneous responsivity owing to the quantum-mechanical geometric phase of electronic states. Nevertheless, the small–band-gap material for the low-energy BPVE inevitably suffers from the thermal noise due to the intrinsically high conductivity. Here, we demonstrate the shift current induced by soft-phonon excitations without creation of electron-hole pairs in the archetypal ferroelectric $BaTiO_3$ by using the terahertz light, whose energy scale is three orders of magnitude smaller than the electronic band gap. At and above room temperature, we observe appreciable photocurrents caused by the soft-phonon excitation as large as that for electronic excitation and their strong phonon-mode dependence. The observed phonon-driven BPVE can be well accounted for by the shift current model, considering the electron–phonon coupling in the displacement-type ferroelectrics, as supported by the first-principles calculation. Our findings establish the efficient quantum BPVE arising from low-energy elementary excitations, suggesting the principle for the high-performance terahertz photodetectors.

bulk photovoltaic effect | terahertz optics | shift current | ferroelectrics

Significance

The quantum-mechanical geometric phase of electrons provides various phenomena such as the dissipationless photocurrent generation through the shift current mechanism. So far, the photocurrent generations are limited to above or near the band-gap photon energy, which contradicts the increasing demand of the low-energy photonic functionality. We demonstrate the photocurrent through the optical phonon excitations in ferroelectric $BaTiO_3$ by using the terahertz light with photon energy far below the band gap. This photocurrent without electron-hole pair generation is never explained by the semiclassical treatment of electrons and only arises from the quantum-mechanical geometric phase. The observed photon-to-current conversion efficiency is as large as that for electronic excitation, which can be well accounted for by newly developed theoretical formulation of shift current.

In the past decade, the essential role of the electronic topology characterized by the geometric phase (i.e., the Berry phase) has been recognized for various classes of electromagnetic phenomena in crystalline solids (1). In addition to the most established framework for the intrinsic anomalous Hall effect in the systems without time-reversal symmetry (2), in recent, extensive, theoretical studies, researchers have investigated the geometrical nature of nonlinear optical effects in the systems without inversion symmetry, including polar or ferroelectric materials (3–7). The shift current is one such mechanism of the bulk photovoltaic effect (BPVE) that is related to the quantum geometric phase of electrons in solids (8–17) and can be the promising principle for the solar cell and photodetector (18, 19). Specifically, the shift current originates from the shift of an electron wave packet in the real space upon the interband optical transition. This shift is quantified by the so-called shift vector that is composed of the Berry connection difference between the valence and conduction bands involved in the optical transition (20, 21). The BPVE by shift current is essentially different from the transport current, producing the less-dissipative energy flow with almost instantaneous response. The shift-current response is generated within the light illumination place and never dependent on the defect density of the material and, therefore, the mobility of the photocarrier (16, 17, 22). Also, the shift current is induced by the exciton excitation (23). This intrinsic mechanism is in contrast to the extrinsic mechanisms such as the ballistic current in the relaxation process of the excited carriers (24–26) as well as the widely used *p-n* junction, where the photocarriers travel to the electrodes via drift-diffusive transport induced by the built-in potential.

The modern theory of ferroelectricity is closely relevant to the intuitive picture of the shift current addressed in this article. The ferroelectric polarization (P) is generally composed of the asymmetry of the valence electronic wavefunction in addition to the displacement of the ions. The former electronic P is formulated by the Berry phase of the valence bands, whose change upon the interband transition is responsible for the shift vector (12, 20, 21). Recent experimental and theoretical studies have, indeed, demonstrated the large shift-current response in various classes of materials hosting the large electronic P (8, 9, 13, 14, 17). The direct connection between the electronic P and shift current indicates that the shift-current generation can be driven by any

Author contributions: N.N., Y. Tokura, and Y. Takahashi designed research; Y.O., T.M., N.O., Y.K., G.-Y.G., M.N., and M.K. performed research; and Y.O., T.M., G.-Y.G., and Y. Takahashi wrote the paper.

The authors declare no competing interest.

This article is a PNAS Direct Submission.

[1]Y.O. and T.M. equally contributed to this work.

[2]To whom correspondence may be addressed. Email: okamura@ap.t.u-tokyo.ac.jp or youtarou-takahashi@ap.t.u-tokyo.ac.jp.

This article contains supporting information online at http://www.pnas.org/lookup/suppl/doi:10.1073/pnas.2122313119/-/DCSupplemental.

Published March 28, 2022.

excitation that is coupled with the electronic states and is able to modulate the electronic P, including low-energy elementary excitations (27, 28). Note, however, that the usual P current cannot be the direct current, in sharp contrast to the shift current studied here. This prospective photocurrent mechanism does not require the electronic interband transition, contrary to many other photovoltaic mechanisms, leading to low-energy photodetection.

Here, we exploit the soft-phonon excitation in displacive-type ferroelectrics to realize this idea. The soft phonon has the same deformation pattern as the ferroelectric state; the softening of phonon frequency is accompanied by enhancement of oscillator strength, which is transferred from the electronic excitation. Therefore, the direct excitation of the soft phonons by the terahertz light modulates the electronic P as well, producing the shift current without creation of electron-hole pairs. On this basis, we targeted a ferroelectric $BaTiO_3$, which is known to host the sizable electronic P (29, 30) and the strong soft-phonon excitations in the terahertz region (<15 meV) (31–33).

Results

The paraelectric cubic structure of the perovskite-type $BaTiO_3$ turns into the ferroelectric tetragonal structure below critical temperature (T_C) ~390 K (Fig. 1*A*) with the spontaneous P along the c axis (Fig. 1*B*), and further successive transitions occur at ~280 K (into orthorhombic phase) and at ~190 K (into rhombohedral phase). The ferroelectricity of this compound is known to have the displacement-type and order-disorder-type transition nature: in the case of the displacement-type transition, the spontaneous P shows up by the relative displacement of the positively and negatively charged ions. Meanwhile, in the order-disorder type of transition, the electric dipoles are present even above the T_C but are disordered. These local electric dipoles are aligned below the T_C, resulting in the macroscopic P. In the tetragonal phase, two distinct phonon excitations associated with these two ferroelectric transitions are observed in the terahertz spectra (Fig. 1 *C* and *D*) (31–33). The optical phonon polarized perpendicular to the spontaneous P is related to the displacement-type transition (Slater mode, $||a$). The broad spectral width represents the strong anharmonicity resulting from the softening of the phonon frequency. On the other hand, the relaxational mode, which has the Debye-type dielectric response polarized along the c axis, is related to the order-disorder type of transition. $BaTiO_3$ is transparent below the large band-gap energy ~3.2 eV, except for the infrared optical phonon excitations (Fig. 1*E*), being consistent with its highly insulating nature. We note that the BPVE for the interband transition in the ultraviolet (UV) region has been extensively studied in this material (8, 34–37). The photocurrent action spectra reported in the seminal work have been recently reproduced by the first-principles calculations (8), suggesting the dominant role of the shift current mechanism for the BPVE.

To pursue the phonon-driven shift current, we measured the photocurrent induced by the terahertz pulse focused on the center of the sample, away from the metal contacts (Figs. 1*F* and 2*A*; *Materials and Methods*). We note that the shift current is generated only within the illumination place but can flow into the electrodes via the capacitive coupling in case of the pulse excitation (14, 16). The linearly polarized terahertz light, whose center photon energy and bandwidth are both ~4 meV (Fig. 1*F*), is suitable for the resonant excitation of two types of soft phonons. The BPVE is generally described by the second-order nonlinear optical conductivity tensor $\sigma^{(2)}$. On the basis of the symmetry consideration, the zzz ($\sigma^{(2)}_{zzz}$) and zxx ($\sigma^{(2)}_{zxx}$) components of the $\sigma^{(2)}$ are allowed in the tetragonal phase (Fig. 1*A* indicates the coordinates); here, we define $j_i = \sigma^{(2)}_{ijk}(\omega)E_jE_k$, where j_i and E_j represent the photocurrent density along the i axis and electric field of light along the j axis, respectively. Accordingly, the $\sigma^{(2)}_{zzz}$ and $\sigma^{(2)}_{zxx}$ describe the photocurrent responses upon the relaxational mode for $E||z(c)$ and upon the Slater mode for $E||x(a)$, respectively.

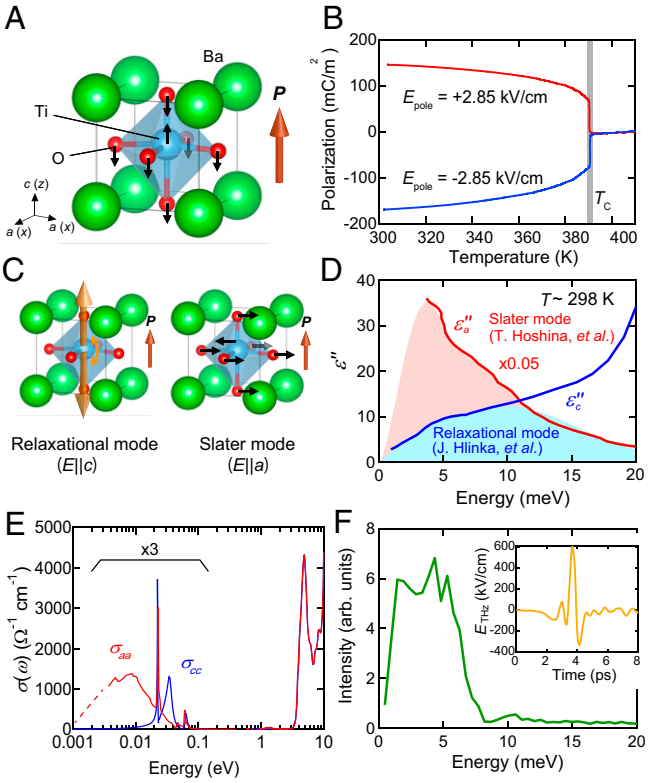

Fig. 1. Static and dynamical ferroelectric nature of tetragonal $BaTiO_3$. (*A*) The crystal structure of the tetragonal phase of $BaTiO_3$. (*B*) Temperature dependence of the spontaneous electric P along the c axis. E_{pole} represents the poling field. (*C*) Schematic illustrations of two kinds of soft phonon modes: relaxational mode for $E||c$ (*Left*) and Slater mode for $E||a$ (*Right*). (*D*) The imaginary part of the terahertz dielectric constants, ε_a'' (red curve) and ε_c'' (blue curve) in the tetragonal phase at room temperature. ε_a'' and ε_c'' spectra are reproduced from refs. 32 and 33, respectively. ε_a'' is multiplied by a factor of 0.05 for clarity. (*E*) The optical conductivity spectra, σ_{aa} (red curve) and σ_{cc} (blue curve) in the wide energy range. The data below 0.1 eV are multiplied by a factor of 3 for clarity. (*F*) The spectral amplitude of the terahertz electric field used in this study. (*Inset*) Time waveform of the terahertz light pulse. Arb, arbitrary.

For the both cases, we observed appreciable zero-bias photocurrent pulses in the single-domain ferroelectric states at room temperature (Fig. 2 *B* and *C*). The signs of the photocurrents are totally reversed by the reversal of the ferroelectric P (red and blue curves in Fig. 2*B*; magenta and light blue curves in Fig. 2*C*). These signals are gradually enhanced with increasing temperature and disappear in the centrosymmetric paraelectric phase (Fig. 2*D*), while the strong soft-phonon excitations exist in terahertz region even above the T_C (31, 33). We note that the photocurrent signal is least observed for the multidomain state with no net P after zero field cooling (gray curve in Fig. 2*B*). Therefore, it is concluded that the observation of photocurrents is produced by the inversion symmetry breaking of the bulk crystal. The magnitude of the photocurrent is proportional to the square of the terahertz electric field (Fig. 2*E*), in accord with the second-order nonlinear effect described by $\sigma^{(2)}_{ijk}$. We

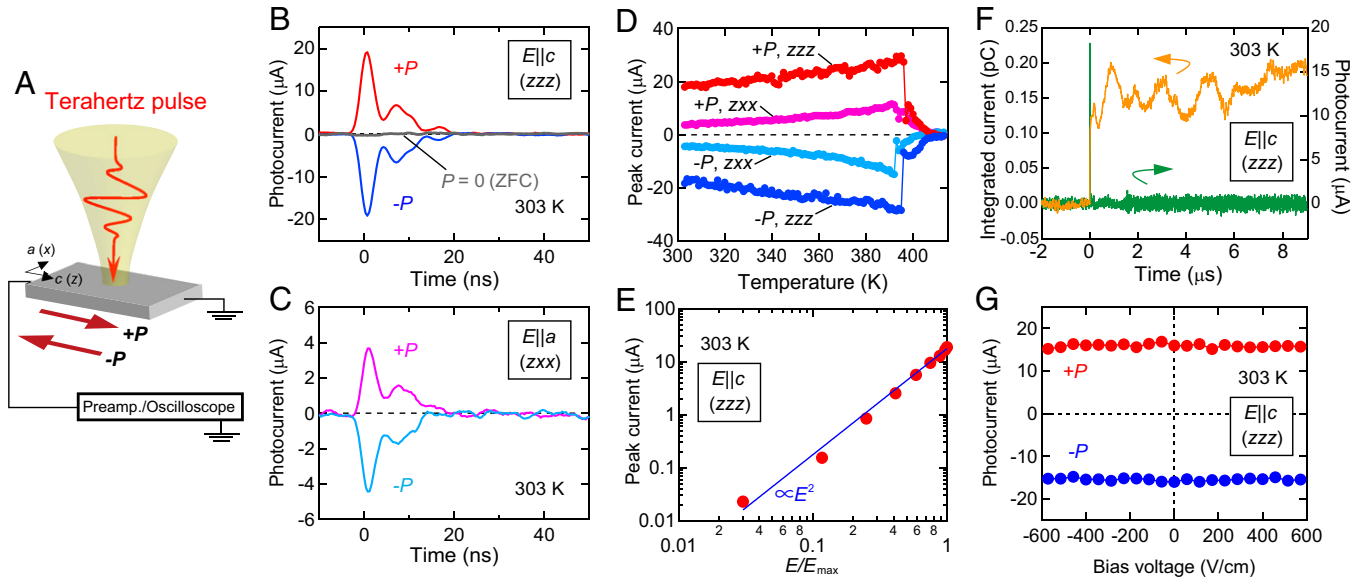

Fig. 2. Terahertz bulk photovoltaic effect. (*A*) Schematic illustration of the experimental setup. (*B* and *C*) Pulsed photocurrent for $E||c$ (*B*) and $E||a$ (*C*). In *B* (*C*), the red (magenta) and blue (light blue) solid curves represent the data at 303 K for *P* states $+P$ and $-P$, respectively. Photocurrent responses for $E||c$ and $E||a$ correspond to the *zzz* and *zxx* components of nonlinear optical conductivity, respectively. The gray curve in *B* represents the photocurrent for the multidomain state after zero field cooling (ZFC). (*D*) Temperature dependence of the peak values of photocurrents for the Slater mode and the relaxational mode. Red (magenta) and blue (light blue) circles denote the *zzz* (*zxx*) components of nonlinear optical conductivity for $+P$ and $-P$ states, respectively. (*E*) Terahertz electric field dependence of the peak value of the photocurrent (red circles) on the log-log scale. The blue line represents the fitting curve using E^2. (*F*) Transient photocurrent response on the long time scale (green curve) and the corresponding integrated current (orange curve). (*G*) The bias-voltage dependence of the peak values of the photocurrent pulses for $+P$ (red circles) and $-P$ (blue circles) states. Preamp, preamplifier.

also found that the light-*P* dependence of the photocurrent shows sine-wave-like behavior (*SI Appendix*, Fig. S1), which confirms the tensorial nature of $\sigma^{(2)}$ and is consistent with the point group ($4mm$) of $BaTiO_3$ at room temperature. All these results manifest the presence of the BPVE without interband transition (i.e., the phonon-driven terahertz shift current).

This scenario is corroborated by the following two observations: First, as seen in Fig. 2*F*, we observed the sharp photocurrent pulse only during the irradiation of the terahertz-light pulse. The time integral of the photocurrent shows the step-function-like behavior, which persists without discernible decay or increase (orange curve in Fig. 2*F*). This observation is consistent with the fact that the shift current is the steady-state photocurrent during the light irradiation with nonvanishing integrated current. This is in contrast to the transient pyroelectric current induced by the instantaneous light-induced heating with zero integrated current in total (for more details of the transient pyroelectric current, see *SI Appendix*, Fig. S2). The other important observation is that the photocurrent signal is independent of the external bias voltage (Fig. 2*G*), indicating that the open circuit voltage is larger than 600 V/cm. Since the open circuit voltage is at most 80 V/cm for the above-band-gap excitation (35), this large open circuit voltage demonstrates the absence of mobile photocarriers generated by the terahertz field. Thus, the diffusive charge transport in the photocurrent generation can be excluded for this terahertz photocurrent generation, as expected for the phonon-driven shift current.

The clear phonon-mode dependence is observed in the nonlinear optical conductivity, which is directly connected to the shift vector (4). We note that the duration of the original photocurrent pulse induced inside the material should be comparable to that of the irradiated terahertz pulse (~1 ps) due to the instantaneous response expected for the shift-current mechanism. However, the electrical circuit used for the ultrafast photocurrent detection inevitably causes the attenuation and broadening of current pulses to ~5 ns, making the quantitative estimation of $\sigma^{(2)}$ difficult. Thus, here we introduce the alternative quantity $\alpha_j J^P_i / I_{abs}$, which is proportional to the nonlinear optical conductivity $\sigma^{(2)}{}_{ijj}$ (*SI Appendix*); α_j, J^P_i, and I_{abs} represent the absorption coefficient for the light *P* along the *j* axis, the peak value of pulsed photocurrent flowing along the *i* axis $J_i(t)$, and the absorbed light power, respectively. In the terahertz region, the *zxx* component (Slater mode, $\alpha_x J^P_z / I_{abs}$) is ~24 times larger than the *zzz* component (relaxational mode, $\alpha_z J^P_z / I_{abs}$) (Fig. 3*A*), demonstrating the strong phonon-mode dependence of the $\sigma^{(2)}$. In contrast, the electronic excitations show the relatively isotropic $\sigma^{(2)}$ spectra, whose magnitudes are comparable to that of the *zxx* component (Slater mode) for the phonon excitation (Fig. 3*B* and *SI Appendix*, Fig. S3). Accordingly, the Slater mode gives rise to the shift current as large as the interband optical transitions.

We also discuss the Glass coefficient (38), which is defined as J/wi_{abs}, where *J*, i_{abs}, and *w* respectively represent the photocurrent, the absorbed light power density, and the width of photo-irradiated area (*SI Appendix*). On the basis of the observed pulse photocurrent value, we roughly estimate the Glass coefficients to be $\sim 1 \times 10^{-8}$ cm/V for two soft-phonon modes, which were found to be comparable to those for the electronic excitations in $BaTiO_3$ (*SI Appendix*, Fig. S4). The Glass coefficient of this material in the UV region is known to be relatively large among other known compounds (15), indicating the high efficiency of the phonon-driven shift current.

Discussion

To understand the mechanism of phonon-driven shift current, we developed a theoretical framework (*SI Appendix*). We considered the Rice–Mele model, which is a famous one-dimensional model for ferroelectrics (12). By taking into account the electron–phonon coupling with strength of *g*, we derived the nonlinear optical conductivity $\sigma^{(2)}$ for the shift current upon the phonon excitation with resonance energy E_{ph} using the diagrammatic technique (39). The magnitude of $\sigma^{(2)}$

is scaled by the square of the strength of the electron–phonon coupling g^2 and inverse phonon energy $1/E_{ph}$; $\sigma^{(2)} \propto g^2/E_{ph}$ (*SI Appendix*, Eq. **S2** for explicit expression). Therefore, the intrinsically small energy of soft phonon should enhance the $\sigma^{(2)}$ upon the phonon excitation, rationalizing the large phonon-driven shift current comparable to the electronic shift current. This minimal theoretical analysis also explains the phonon-mode dependence of $\sigma^{(2)}$. The nonlinear conductivity can be rewritten as $\sigma^{(2)} = \frac{e}{E_{ph}}\sigma^{(1)}R$ using the linear optical conductivity $\sigma^{(1)}$ and the shift vector R representing the real-space shift of the electronic wavefunction for the phonon excitation. The magnitude of $\sigma^{(1)}$ for the Slater mode is ~70 times larger than that for the relaxational mode at ~4 meV. If these modes have comparable shift vector R, this accounts for the strong anisotropy of $\sigma^{(2)}$, as experimentally observed.

On the basis of the formalism established here, we calculate the $\sigma^{(2)}_{zxx}$ due to the Slater mode using the density functional theory (*SI Appendix*). The magnitude of the $\sigma^{(2)}_{zxx}$ due to the Slater mode is comparable to or larger than that of the electronic excitation near the band gap, and the sign of the $\sigma^{(2)}_{zxx}$ is opposite to that of the electric P direction (Fig. 4). These facts reasonably explain the experimental observation, which demonstrates the dominant role of the shift-current mechanism mediated by the electron–phonon interaction. Although the radiative relaxation of phonon can reduce the photocurrent through the backflow of shift current, the short lifetime of soft phonons (<1 ps), which can be deduced from the line width, suggests that the nonradiative relaxation is dominant and the reduction resulting from this backflow is negligible. The extrinsic mechanisms arising from the interaction between the phonons and from the impurity scattering may also contribute to the terahertz photocurrent.

Photodetection of the terahertz/far-infrared light is relevant to a variety of applications, including sensing, imaging, and communication. The conventional low-energy photodetection relies on the photocarrier generation in the small–band-gap materials, on the photo-induced thermalization of the systems, or on the superconducting tunnel junction (18, 19), which usually cannot ensure high-speed and low-noise responses with the room-temperature operation (*SI Appendix*). In this context, the phonon-driven shift current provides the prominent principle for the low-energy

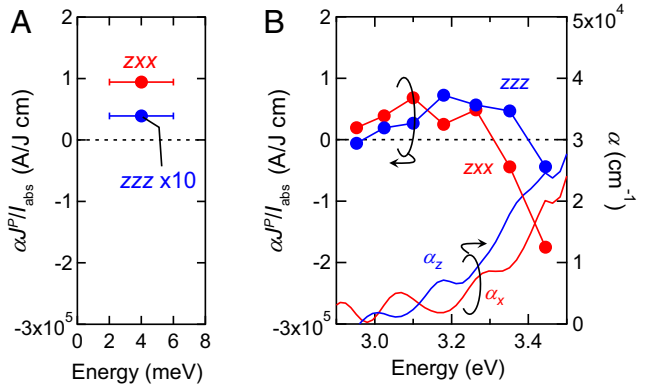

Fig. 3. Nonlinear optical conductivity spectra for phonon and electronic excitations. (*A* and *B*) The *zxx* (red circles) and *zzz* (blue circles) components of $\alpha J^P/I_{abs}$, which respectively quantify the nonlinear optical conductivities $\sigma^{(2)}_{zxx}$ and $\sigma^{(2)}_{zzz}$ in terahertz (*A*) and visible/UV regions (*B*). α, J^P, and I_{abs} represent the absorption coefficient, peak value of pulsed photocurrent, and absorbed light power, respectively. In calculating the terahertz $\alpha J^P/I_{abs}$, we used the α at 4 meV obtained from refs. 32 and 33. The horizontal bars shown in panel *A* denote the bandwidth of the terahertz light. On the right axis of *B*, we show the absorption spectra α_x (red curve) and α_z (blue curve).

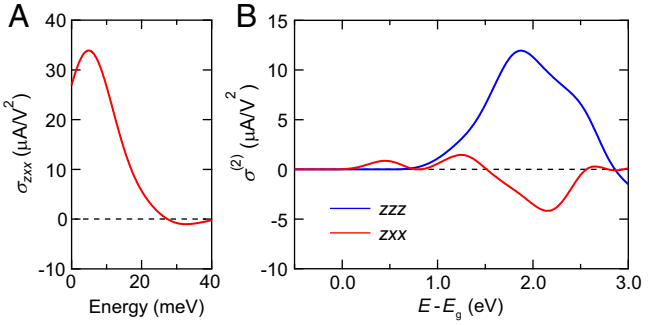

Fig. 4. The shift-current conductivity from first-principles calculations. (*A*) Calculated shift-current response due to the phonon excitation with broadening Γ = 10 meV. (*B*) Calculated shift-current response due to the electronic excitation with carrier lifetime broadening Γ = 0.1 eV. E and E_g, shown on the horizontal axis of *B*, represent the photon energy and band gap, respectively. Here, we define the photocurrent opposite to the electric-P direction as positive.

photodetection, which can realize almost instantaneous response and significant reduction of the thermal noise, due to the absence of conduction carriers even at room temperature. Although the figure of merit, such as noise-equivalent power obtained in this experiment, is still below that of the commercially available detectors (*SI Appendix*), the optimization in the form of the device will increase the performance of terahertz detection. Our present work proves the phonon-driven shift current without creation of real electron-hole pairs, which demonstrates the crucial importance of the geometrical nature of inversion-broken materials for efficient photocurrent generation. The phonon excitation may be strongly coupled to the topological electronic structure in particular materials, which will open up an avenue to control the topological nature of matter and enhance the terahertz photoresponsivity through the combination of intense geometrical phase and strong electron–phonon interaction (40–45). These findings lead to a principle for low-energy photodetectors operated irrespective of the band gap and stimulate additional research for unexplored topological quantum phenomena with promising functionality.

Materials and Methods

Single Crystal Growth. The single crystalline samples of $Ba_{0.97}Sr_{0.03}TiO_3$ were grown by the laser floating zone method (46). Here, Sr is dilutely doped for a technical reason: a large single crystal can be acquired by avoiding the incorporation of hexagonal (nonperovskite) crystal structural phase during the crystal growth.

Electric *P* Measurement. The electric P is deduced by measuring the pyroelectric current while increasing the temperature. The single-domain state is stabilized by field cooling from ~410 K, which is well above T_C, with application of the electric field of ±2.85 kV/cm. The almost single ferroelectric-domain formation by the electric-field poling confirms that the voltage is applied uniformly over the entire sample region. We also note that the sample is well insulating and the resistance cannot be measured.

Intense Terahertz Pulse Generation. For a light source, we used a regenerative amplified Ti:sapphire laser system with a pulse energy of 5 mJ, pulse duration of 100 fs, repetition rate of 1 kHz, and the center wavelength of 800 nm. The intense terahertz pulses were generated by the tilted-pulse front method with a $LiNbO_3$ crystal (47). The spot size was approximately 1 mm. The time waveform of the terahertz pulse is measured by the electro-optic sampling technique using a ZnTe (110) crystal. The intensity of the terahertz light is controlled by using wire grid polarizers. Except for investigating the terahertz-electric-field dependence (Fig. 2*E*), we used the terahertz pulse with the maximal intensity shown in Fig. 1*F*. The terahertz power was estimated using a power meter (T-RAD, Gentec-EO).

UV Light Generation. We used the second harmonic generation of the near-infrared/visible light from an optical parametric amplifier pumped by a Yb-based amplified laser with a pulse energy of 0.833 mJ, pulse duration of ∼140 fs, and repetition rate of 6 kHz. The spot size was approximately 1 mm.

Pulsed Photocurrent Measurement. We used an oscilloscope to measure the pulsed photocurrent signal for each light pulse. The bandwidth of the preamplifier was 200 MHz. Typically, the size of the top surface of the sample is 2.5 × 3 mm^2 and thickness is 1 mm. We shined the light at the center of the sample and carefully covered the electrodes with aluminum foil to eliminate spurious effects. The photocurrent pulse duration was determined presumably by the bandwidth of the preamplifier (200 MHz), as indicated by the duration of the main photocurrent pulse (∼5 ns). Meanwhile, we also observed the similar-shaped secondary and even tertiary pulse signals, leading to a more broadened pulse. These parasitic signals are known as the ringing effect, which inevitably occurs for a short electrical pulse, due to the parasitic capacitances and inductances (and impedance mismatch) in the circuit. We note that this oscillatory parasitic signal is not relevant to the piezoelectric effect induced by the coherent phonon excitation because the same waveform of transient photocurrent is observed for UV pulse excitations (*SI Appendix*, Fig. S3).

Optical Conductivity and Absorption Spectra. Polarized optical conductivity and absorption spectra above 0.07 eV were obtained through the Kramers–Kronig analysis of the reflectivity spectra. We measured the reflectivity spectra using a Fourier transform–type spectrometer in the infrared region above 0.07 eV and a mononchromator-type spectrometer in the visible and UV regions below 4.1 eV. The reflectivity data above 4.1 eV were taken from ref. 48. We calculated σ_{aa} and σ_{cc} spectra below 0.07 eV from the dielectric constants shown in ref. 32 and ref. 33, respectively.

Data Availability. All study data are included in the article and/or *SI Appendix*.

ACKNOWLEDGMENTS. We thank S. Sawamura, M. Ogino, and J. Fujioka for experimental help. G.-Y.G. thanks Samual Poncé for helpful communications on the Electron–Phonon coupling using Wannier functions (EPW) program. This work was partially supported by Japan Science and Technology Agency Core Research for Evolutional Science and Technology (Grants JPMJCR16F1 and JPMJCR1874). N.N. is supported by Japan Society for the Promotion of Science Grants-in-Aid for Scientific Research (JSPS KAKENHI) Grant 18H03676. Y. Takahashi is supported by JSPS KAKENHI Grant 21H01796. G.-Y.G. is supported by the Ministry of Science and Technology, the National Center for High-Performance Computing, and the Center for Emergent Materials and Advanced Devices, National Taiwan University, Taiwan.

Author affiliations: [a]Department of Applied Physics and Quantum Phase Electronics Center, University of Tokyo, Tokyo 113-8656, Japan; [b]PRESTO, Japan Science and Technology Agency, Tokyo 113-8656, Japan; [c]RIKEN Center for Emergent Matter Science, Wako 351-0198, Japan; [d]Department of Physics, National Taiwan University, Taipei 10617, Taiwan; [e]Physics Division, National Center for Theoretical Sciences, Taipei 10617, Taiwan; and [f]Tokyo College, University of Tokyo, Tokyo 113-8656, Japan

1. D. Xiao, M.-C. Chang, Q. Niu, Berry phase effect on electronic properties. *Rev. Mod. Phys.* **82**, 1959 (2010).
2. N. Nagaosa, J. Sinova, S. Onoda, A. H. MacDonald, N. P. Ong, Anomalous Hall effect. *Rev. Mod. Phys.* **82**, 1539 (2010).
3. B. I. Sturman, V. M. Fridkin, *The Photovoltaic and Photorefractive Effects in Noncentrosymmetric Materials* (Gordon and Beach Science Publishers, Philadelphia, PA, 1992).
4. T. Morimoto, N. Nagaosa, Topological nature of nonlinear optical effects in solids. *Sci. Adv.* **2**, e1501524 (2016).
5. L. Wu *et al.*, Giant anisotropic nonlinear optical response in transition metal monopnictide Weyl semimetal. *Nat. Phys.* **13**, 350 (2017).
6. J. Ahn, G.-Y. Guo, N. Nagaosa, Low-frequency divergence and quantum geometry of the bulk photovoltaic effect in topological semimetals. *Phys. Rev. X* **10**, 041041 (2020).
7. Q. Ma, A. G. Grushin, K. S. Burch, Topology and geometry under the nonlinear electromagnetic spotlight. *Nat. Mater.* **20**, 1601–1614 (2021).
8. S. M. Young, A. M. Rappe, First principles calculation of the shift current photovoltaic effect in ferroelectrics. *Phys. Rev. Lett.* **109**, 116601 (2012).
9. I. Grinberg *et al.*, Perovskite oxides for visible-light-absorbing ferroelectric and photovoltaic materials. *Nature* **503**, 509–512 (2013).
10. L. Z. Tan *et al.*, Shift current bulk photovoltaic effect in polar materials–Hybrid and oxide perovskites and beyond. *npj Comput. Mater.* **2**, 16026 (2016).
11. L. Braun *et al.*, Ultrafast photocurrents at the surface of the three-dimensional topological insulator Bi_2Se_3. *Nat. Commun.* **7**, 13259 (2016).
12. B. M. Fregoso, T. Morimoto, J. E. Moore, Quantitative relationship between polarization difference and the zone-averaged shift photocurrent. *Phys. Rev. B* **96**, 075421 (2017).
13. M. Nakamura *et al.*, Shift current photovoltaic effect in a ferroelectric charge-transfer complex. *Nat. Commun.* **8**, 281 (2017).
14. N. Ogawa, M. Sotome, Y. Kaneko, M. Ogino, Y. Tokura, Shift current in the ferroelectric semiconductor SbSI. *Phys. Rev. B* **96**, 241203 (2017).
15. G. B. Osterhoudt *et al.*, Colossal mid-infrared bulk photovoltaic effect in a type-I Weyl semimetal. *Nat. Mater.* **18**, 471–475 (2019).
16. M. Nakamura *et al.*, Non-local photocurrent in a ferroelectric semiconductor SbSI under local photoexcitation. *Appl. Phys. Lett.* **116**, 122902 (2020).
17. H. Hatada *et al.*, Defect tolerant zero-bias topological photocurrent in a ferroelectric semiconductor. *Proc. Natl. Acad. Sci. U.S.A.* **117**, 20411–20415 (2020).
18. A. Rogalski, Progress in focal plane array technologies. *Prog. Quantum Electron.* **36**, 342 (2012).
19. J. Liu, F. Xia, D. Xiao, F. J. García de Abajo, D. Sun, Semimetals for high-performance photodetection. *Nat. Mater.* **19**, 830–837 (2020).
20. D. Vanderbilt, R. D. King-Smith, Electric polarization as a bulk quantity and its relation to surface charge. *Phys. Rev. B Condens. Matter* **48**, 4442–4455 (1993).
21. R. Resta, Macroscopic polarization in crystalline dielectric: The geometric phase approach. *Rev. Mod. Phys.* **66**, 899 (1994).
22. H. Ishizuka, N. Nagaosa, Theory of bulk photovoltaic effect in Anderson insulator. *Proc. Natl. Acad. Sci. U.S.A.* **118**, e2023642118 (2021).
23. M. Sotome *et al.*, Terahertz emission spectroscopy of ultrafast exciton shift current in the noncentrosymmetric semiconductor CdS. *Phys. Rev. B* **103**, L241111 (2021).
24. B. I. Sturman, V. M. Fridkin, *Photovoltaic and Photorefractive Effects in Noncentrosymmetric Materials* (CRC Press, Philadelphia, PA, 1992).
25. V. I. Belinicher, E. Ivchenko, B. I. Sturman, Kinetic theory of the shift photovoltaic effect in piezoelectrics. *Zh. Eksp. Teor. Fiz.* **83**, 649 (1982).
26. V. I. Belinicher, B. I. Sturman, The photogalvanic effect in media lacking a center of symmetry. *Sov. Phys. Usp.* **23**, 199 (1980).
27. T. Morimoto, N. Nagaosa, Topological aspects of nonlinear excitonic process in noncetrosymmetric crystals. *Phys. Rev. B* **94**, 035117 (2016).
28. T. Morimoto, N. Nagaosa, Shift current from electromagnon excitations in multiferroics. *Phys. Rev. B* **100**, 235138 (2019).
29. R. Cohen, Origin of ferroelectrics in perovskite oxides. *Nature* **358**, 136 (1992).
30. Ph. Ghosez, X. Gonze, J. P. Michenaud, First principle calculations of dielectric and effective charge tensors in barium titanate. *Ferroelectrics* **153**, 91 (1994).
31. Y. Luspin, J. L. Servoin, F. Grvais, Soft mode spectroscopy in barium titanate. *J. Phys. Chem.* **13**, 3761 (1980).
32. T. Hoshina, K. Kanehara, H. Takeda, T. Tsurumi, Terahertz dielectric response of single-domain $BaTiO_3$ measured by far-infared spectroscopic ellipsometry. *Jpn. J. Appl. Phys.* **53**, 09PD03 (2014).
33. J. Hlinka *et al.*, Coexistence of the phonon and relaxation soft modes in the terahertz dielectric response of tetragonal $BaTiO_3$. *Phys. Rev. Lett.* **101**, 167402 (2008).
34. W. T. H. Koch, R. Munser, W. Ruppel, P. Würfel, Anomalous photovoltage in $BaTiO_3$. *Ferroelectrics* **13**, 305 (1976).
35. W. T. H. Koch, R. Munser, W. Ruppel, P. Würfel, Bulk photovoltaic effect in $BaTiO_3$. *Solid State Commun.* **17**, 847 (1975).
36. J. E. Spanier *et al.*, Power conversion efficiency exceeding the Shockley-Queisser limit in a ferroelectric insulator. *Nat. Photonics* **10**, 611 (2016).
37. Z. Gu *et al.*, Mesoscopic free path of nonthermalized photogenerated carriers in a ferroelectric insulator. *Phys. Rev. Lett.* **118**, 096601 (2017).
38. A. M. Glass, D. von der Linde, T. J. Negran, High-voltage bulk photovoltaic effect and the photorefractive process in $LiNbO_3$. *Appl. Phys. Lett.* **25**, 233 (1974).
39. D. E. Parker, T. Morimoto, J. Orenstein, J. E. Moore, Diagrammatic approach to nonlinear optical response with approach to Weyl semimetals. *Phys. Rev. B* **99**, 045121 (2019).
40. B. Xu *et al.*, Temperature-tunable Fano resonance induced by strong coupling between Weyl fermions and phonons in TaAs. *Nat. Commun.* **8**, 14933 (2017).
41. J. Coulter *et al.*, Uncovering electron-phonon scattering and phonon dynamics in type-I Weyl semimetals. *Phys. Rev. B* **100**, 220301 (2019).
42. D. Wulferding *et al.*, Effect of topology on quasiparticle interactions in the Weyl semimetal WP_2. *Phys. Rev. B* **102**, 075116 (2020).
43. G. B. Osterhoudt *et al.*, Evidence for dominant phonon-electron scattering in Weyl semimetal WP_2. *Phys. Rev. X* **11**, 011017 (2021).
44. H.-Y. Yang *et al.*, Evidence of a coupled electron-phonon liquid in $NbGe_2$. *Nat. Commun.* **12**, 5292 (2021).
45. L. Luo *et al.*, A light-induced phononic symmetry switch and giant dissipationless topological photocurrent in $ZrTe_5$. *Nat. Mater.* **20**, 329–334 (2021).
46. Y. Kaneko, Y. Tokura, Floating zone furnace equipped with a high power laser of 1kW composed of five smart beams. *J. Cryst. Growth* **533**, 125435 (2020).
47. H. Hirori, A. Doi, F. Blanchard, K. Tanaka, Single-cycle terahertz pulses with amplitudes exceeding 1 MV/cm generated by optical rectification in $LiNbO_3$. *Appl. Phys. Lett.* **98**, 091106 (2011).
48. M. Cardona, Optical properties and band structure of $SrTiO_3$ and $BaTiO_3$. *Phys. Rev.* **140**, A651 (1965).